JOURNAL OF NANOMATERIALS AND DEVICES
Jul - Dec 2026, VOL. 4, ISSUE 2, pp. 36-49
https://doi.org/10.61577/jnd.2026.100009

RESEAPRO JOURNALS

ORIGINAL ARTICLE

OPEN ACCESS

Crystallographic integration of surface control-induced silver nanoparticles: Nucleation and crystal growth mechanism analysis insights

Sumaiya Islam Sadia[1], Kamrun Nahar[1], Mohshin Maola[1], Sukanta Mondal[1], Md. Ashraful Alam[2], Sharif Md. Al-Reza[1], Raton Kumar Bishwas[2] and Shirin Akter Jahan[2]

[1] Applied Chemistry and Chemical Engineering, Islamic University, Bangladesh
[2] Institute of Glass and Ceramic Research and Testing, Dhaka, Bangladesh

ABSTRACT

Highly crystalline silver nanoparticles (Ag NPs) were synthesized using an eco-friendly sol–gel method with ascorbic acid as the reducing agent, promoting crystal growth. The influence of washing media-ethanol alone (Y) versus 1:1 ethanol with distilled water (X) was investigated to control surface energy and optimize crystallographic analysis. The X-ray diffraction (XRD) and Rietveld refinement evaluated the X medium, which resulted in a lower crystallite size of 52.3 nm, lattice parameter a=b=c= 4.093 Å, intrinsic stress of 0.08201 GPa, specific surface area of 10.11 m^2/g, and surface-to-volume ratio of 10.7 × 10^7. In contrast, the Y medium exhibited a crystallite size of 73.36 nm, lattice parameter a=b=c= 4.087 Å, intrinsic stress 0.02743 GPa, specific surface area 6.43 m^2/g, and surface-to-volume ratio 6.74 × 10^7. The Rietveld analysis confirmed a 100 % crystalline Ag phase in X and 91.8 % in Y. The TEM-determined average particle size ranged from 50.17 to 53.32 nm, and SAED confirmed the highly crystalline orientation on the (111) plane in 0.238 nm d-spacing. These crystallinity and structural enhancements significantly impact photocatalytic activity, achieving 82.69 % degradation of methylene blue dye (MBD) under halogen light. The results demonstrate that a simple modification of the washing medium can effectively tailor the crystallinity, phase purity, and surface characteristics of Ag NPs.

KEYWORDS

Reducing agent, Nucleation and growth mechanism, Photocatalysis, Silver nanoparticles (Ag NPs), SAED, TEM

ARTICLE HISTORY

Received 30 August 2026;
Accepted 22 September 2026;
Published 30 September 2026

Introduction

Nanoparticles (NPs) have become integral to advanced science and technology due to their high surface-to-volume ratio and size-dependent properties [1]. Among them, Ag NPs have drawn significant attention for their applications in catalysis, antimicrobial agents, sensing, and environmental remediation [2,3]. The functional performance of Ag NPs is highly dependent on their crystalline structure, particle size, surface defects, and morphology [4,5]. The sol-gel method is a well-established wet-chemical route for synthesizing metallic NPs, offering advantages such as low-temperature processing, homogeneous particle formation, and ease of phase control [6,7]. Previous studies have demonstrated that the sol-gel technique allows the fine-tuning of particle size and crystallinity by adjusting synthesis parameters such as precursor concentration, pH, and temperature [8,9]. For example, Jeon et al. and Shahjahan et al. successfully synthesized Ag NPs using reducing agents such as ascorbic acid and reported uniform particle dispersion [10,11]. Similarly, Gotić and Musić optimized sol-gel conditions to control the phase formation [12]. However, despite these advances, a critical post-synthesis factor remains largely unexplored. The role of washing or dispersion media in controlling the crystallographic and surface properties of Ag NPs. Most existing works focus primarily on precursor optimization [13-15], whereas the influence of solvent polarity, dielectric behavior, and hydrogen bonding during the washing process on the final crystal structure and functionality of Ag NPs has received limited attention [16,17]. Washing media such as ethanol or ethanol-water mixtures can directly impact surface energy during crystallization, which in turn affects nucleation, crystal orientation, and preferential growth [18,19]. For instance, Blazhynska et al. and Pryshchepa et al. highlighted that solvent-particle interactions alter crystallization pathways in sol-gel-derived nanostructures and nanocrystals [20,21].

However, few studies have specifically applied this understanding to Ag NPs. Here, a clear gap exists regarding the surface chemistry dynamics during post-synthesis processing and their influence on NPs' performance. Post-synthesis washing and redispersion can influence the surface chemistry, dispersion behavior, and morphological stability of silver nanocubes, depending on the solvent used [22]. The choice of solvent can influence the stability, morphology, and optical response of surfactant-stabilized silver nanoparticles [23]. The manuscript offers some insight into the use of washing media as a simple and effective method to control the crystallographic properties and photocatalytic performance of silver nanoparticles. The results show that ethanol–water washing can enhance the phase purity, particle dispersion and surface characteristics of the sample, with 82.69 % degradation of methylene blue by the sample performed in 180 min under halogen light. This study emphasizes the role of post synthesis processing in the nanomaterial engineering and provides a feasible method to prepare effective material for environmental remediation. The current study addresses this limitation by systematically investigating the effects of two different washing conditions, ethanol only (sample Y) and a 1:1 ethanol-distilled water mixture (sample X), on the crystallographic, structural, and photocatalytic properties of sol-gel-derived Ag NPs. While the sol-gel synthesis of Ag NPs itself is not novel, our work introduces a new dimension by correlating solvent polarity with surface energy modification and resultant changes in crystallite size, lattice strain, dislocation density, and phase purity. Notably, the combination produced NPs with improved crystallinity, smaller crystallite size, higher intrinsic distortion, phase purity, and enhanced photocatalytic efficiency compared to the two media [24]. This

***Correspondence:** Mr Md. Ashraful Alam, Institute of Glass and Ceramic Research and Testing, Dhaka, Bangladesh. e-mail: ashrafulalam@bcsir.gov.bd

© 2026 The Author(s). Published by Reseapro Journals. This is an Open Access article distributed under the terms of the Creative Commons Attribution License (http://creativecommons.org/licenses/by/4.0/), which permits unrestricted use, distribution, and reproduction in any medium, provided the original work is properly cited.

relationship between washing medium and material performance has not been previously reported in detail for Ag NPs [25-28]. Although solvent-mediated crystallization effects have been reported for various NPs, their specific influence during the post-synthesis washing stage of sol-gel-derived Ag NPs remains comparatively less explored [29]. Previous studies mainly focused on precursor chemistry, morphology control, and solvent interactions without clearly correlating post-synthesis washing conditions with crystallographic and photocatalytic properties of Ag NPs [30]. In contrast, this study demonstrates that polarity-controlled washing media significantly influence nucleation, lattice strain, phase purity, surface area, and photocatalytic efficiency. Furthermore, the simple modification of the washing medium can significantly influence particle dispersion, crystallinity, lattice characteristics, and photocatalytic degradation efficiency. The novelty of this investigation is the post-synthesis washing medium as a key factor influencing the phase purity, crystallographic properties, and photocatalytic performance of Ag NPs, supported by comprehensive Rietveld refinement, WPPF, and multi-model crystallographic analysis. The ethanol–water washed sample achieved 100 % FCC phase purity, and the degradation of methylene blue also lies in demonstrating that a simple variation in washing media can serve as a powerful surface-control mechanism to engineer crystallinity and functionality in metallic Ag NPs, using a low-cost, scalable, and environmentally friendly approach.

Materials

Silver nitrate ($AgNO_3$), ascorbic acid ($C_6H_8O_6$), and ethanol (C_2H_5OH) were purchased from Sigma-Aldrich [Germany] and used without further purification. Deionized (DI) water was used throughout the experiment that collected from the IPCRD, BCSIR plant.

Methods and Synthesis Route

Ag NPs were synthesized using a modified sol–gel-assisted wet chemical reduction method. The developed approach is also simple, eco-friendly, low-cost, and potentially scalable for environmental applications [31,32]. The method is illustrated in Figure 1. The stoichiometric amount of precursor silver nitrate ($AgNO_3$) in a 1.0 mM (w/v) solution was placed in a 250.0 mL beaker and heated at 80.0 °C [Bioevopeak, China] under continuous stirring at 300.0 rpm. The precursor concentration of 1.0 mM was selected to ensure controlled nucleation and uniform growth of Ag NPs while minimizing particle agglomeration. A moderate concentration also promotes better colloidal stability and homogeneous particle distribution [33].

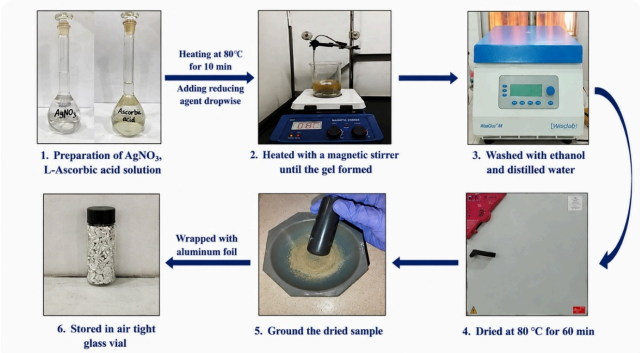


Figure 1. Preparation route of Ag NPs.

When the solution warmed, a 1.0 % (w/v) ascorbic acid ($C_6H_8O_6$) solution was slowly added until the color changed from colorless to yellowish-brown, confirming the reduction of Ag^+ ions and the formation of Ag NPs. The ascorbic acid was employed as a mild reducing agent due to its environmentally friendly nature and ability to produce stable NPs under controlled reaction conditions. The reaction mixture was then heated for an additional 30 to 60 min to form a gel. The reaction temperature of 80.0 °C was chosen to accelerate the reduction kinetics and enhance NPs crystallization, while preventing rapid uncontrolled particle growth. The reaction time of 30 to 60 min was optimized to ensure complete reduction of Ag^+ and proper gel formation [34]. Afterward, the gel was cooled to room temperature and washed several times using ethanol and distilled water in a centrifugation at 8000.0 rpm for 20.0 min [Herolab, Germany]. The repeated washing steps were performed to remove unreacted precursors and residual organic impurities, thereby improving the purity of the synthesized Ag NPs [35]. The residue was then dried at 80.0 ºC [ED115, BINDER, USA] in an oven for 60.0 min. After drying, the sample was placed in a desiccator at room temperature, and the dried sample was ground using a mortar. Finally, the product was collected and stored in a glass vial wrapped with aluminum foil to avoid light-induced and atmospheric oxidation.

Characterization

X-ray diffraction

The crystallographic characteristics of the prepared Ag NPs powder were explained using the XRD technique [36]. X-ray reflectometry (XRR) is a non-destructive analytical technique that utilizes the interplay between X-ray radiation and the periodic configuration of atoms in crystalline materials [37]. XRD is also used to determine the crystallographic size, d-spacing, structure, shape, dislocations, density, and lattice parameters [38]. The X-ray generator source is a copper tube that uses a voltage of 40 kV × 50 mA [2.0 kW] by SmartLab SE [Rigaku, Japan]. With a standard incident primary beam and K_β filter 1D for Cu in Bragg-Brentano (BB) optics geometry, the main X-ray passes the Beryllium (Be) window. The Smartlab Studio II [Rigaku, Japan] assessed the data with the *ICDD PDF5+* database. The "Scherrer equation" was used to calculate crystallite size based on XRR data [39-41]. *Equation*

$$D = \frac{K\lambda}{\beta cos\theta} \quad (1)$$

D means crystallite size, λ means wavelength (Cu tube; λ= 0.1541 nm), K means shape factor (=0.9), the full width at half maximum (FWHM) is β, and the diffraction angle is θ. The dislocation density is calculated by the following formula [42].

$$\text{Dislocation density, } \delta = \frac{1}{D^2} \quad (2)$$

Where δ is the dislocation density, and D is the size of the crystallite. Bragg's law is used to calculate the d-spacing values or the interplanar distance between the atoms [43].

UV spectrophotometry

The optical properties were investigated using a spectrophotometer [Shimadzu, UV-1800, Japan] in the UV-visible range. The wavelength range was 300.0 to 800.0 nm, and the absorbance was 0 to 4 absorbance units. The Tauc plot method is based on the idea that the following equations may

© 2026 Reseapro Journals
https://doi.org/10.61577/jnd.2026.100009

accurately represent the energy-dependent absorption coefficient [22].

$$(\alpha.\ h\nu)^{1/\gamma} = B\ (h\nu\text{-}E_g)\ (3)$$

The band gap was determined from the UV–Vis diffuse reflectance spectra using the Kubelka–Munk function and Tauc plot, where (hυ) was plotted against $(\alpha h\nu)^{\gamma}$. The Kubelka-Munk theory can be used to convert the reflectance spectra into corresponding absorption spectra

$$F(R_\infty) = \frac{K}{S} = \frac{(1-R_\infty)^2}{R_\infty} \quad (4)$$

Where **F (R∞)** refers to the Kubelka–Munk function, **R∞** refers to absolute diffuse reflectance, K means absorption coefficient, and S means scattering coefficient. By substituting F R_∞ for α in Eq. 3, the formulation shown in Equation 5.

$$(F(R_\alpha)\,h\nu)^{\frac{1}{\gamma}} = B\left(h\nu - E_g\right) \quad (5)$$

X-axis intersection points of the linear fit in a Tauc plot are used to estimate the band gap energy. By determining the energy levels linked to electronic transitions for synthesized Ag NPs.

Dynamic light scattering and zeta potential

Dynamic light scattering (DLS) is used for determining the average hydrodynamic diameter and size distribution based on the velocity of Brownian motion [44,45]. The Stokes-Einstein equation is used to calculate the hydrodynamic diameter, and the surface charge is quantified using a zeta potential report, which is represented by the Greek letter zeta (ζ). Zeta potential [Zetasizer Ultra, Malvern Panalytical, UK] was introduced to assess the stability of the materials that were developed [42,43]. The autocorrelation function of the photocurrent at a fixed angle is recorded by directing monochromatic light through the sample cell [42,43]. The Zeta potential analyzer [ZSU5700, Malvern Panalytical, UK] was used for this investigation.

Transmission electron microscopy

Transmission electron microscopy (TEM) was conducted by JEM 2100 Plus [JEOL, Japan] for the internal characteristics of the NPs. The LaB_6 filament at 200.0 kV and 104.50 uA was used; 62.0 %, coarse 5 and fine 6, spot size 3, and alpha 3 in the bright-field capturing method were explored. The single tilt sample holder [EM-21010/21020] was introduced [x 62539, y -211.3, z -0.5 and tilt x 0.00]. The detection system of the camera in flash mode was explored [exposure time 1.00 sec].

Photo-catalysis activity

During the observation period [January 2025], the study was recorded at room temperature 23.0 °C, with a distance of 1.0 ft, a halogen radiation frequency of 50.0 Hz, SQ of 500, FL of 500.0 W, and an intensity of 44. The dye solution was generated at a concentration of 20.0 ppm and tested at 10.0 ppm. The dose of catalyst, such as Ag NPs, was 50.0 mg. Absorbance at maximum wavelength **λ**max= 664.50 nm was measured using a UV spectrophotometer [UV-1800 Shimadzu, Japan] at intervals of 0.0, 20.0, 40.0, 60.0, 80.0, 100.0, 120.0, 140.0, 160.0, and 180.0 minutes.

Results and Discussion

Crystallographic phase analysis

The XRD patterns confirm the formation of highly crystalline Ag NPs through the analysis of Bragg positions, intensities, and Miller indices. The main Bragg diffraction observed in the synthesized Ag NPs (X and Y) corresponds to the angles of 37.98° (111), 44.14° (200), 64.20° (220), 77.08° (311), and 81.21° (222) from Ag standard data [ICDD Card No: 04-002-1347]. In Figure 2, X displays distinct diffraction at 37.91°, 44.09°, 64.25°, 77.23°, and 81.38°, which align with (111), (200), (220), (311), and (222) planes, respectively, confirming the metallic Ag crystalline phase.

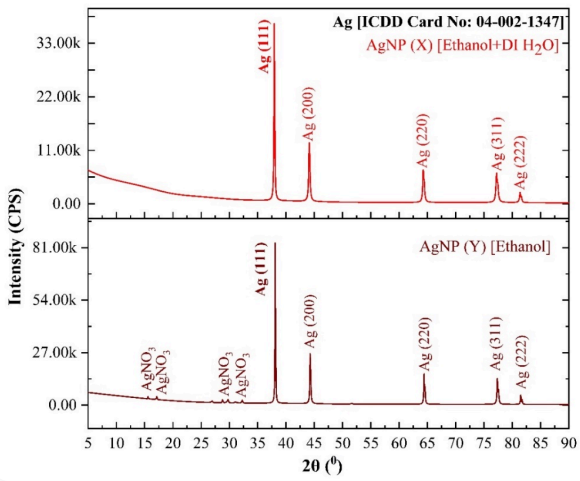


Figure 2. XRD pattern of Ag NPs altering washing medium.

Similarly, sample Y exhibits diffraction at 38.08°, 44.26°, 64.4°, 77.36°, and 81.49°, which align with the (111), (200), (220), (311), and (222) planes, respectively confirming the metallic Ag crystalline phase with the same Miller indices to the zone axis. Additionally, sample Y shows diffraction at 15.58°, 17.13°, 29.74°, and 32.26° responsible for the silver nitrate phase as impurities or unreacted in the solution that inhibit crystal growth. Thus, sample X exclusively shows the metallic Ag crystalline phase, whereas sample Y exhibits minor silver nitrate peaks at 15.58°, 17.13°, 29.74°, and 32.26°. The ethanol–water washing system in sample X therefore provides superior phase purity by effectively removing residual ions and organic impurities due to its enhanced polarity and hydrogen-bonding capacity [21].

Table 1. Grain size calculation of Ag NPs.

2θ (deg)	θ (deg)	FWHM (radians)	Crystal size, D (nm)	d-spacing (nm)	Intensity,I (cps°)	(h k l)
X						
37.91	18.96	0.002147	71.10	0.2371	6118	(1 1 1)
44.09	22.05	0.003159	49.60	0.2052	3008	(2 0 0)
64.25	32.13	0.003508	48.80	0.1448	1945	(2 2 0)
77.23	38.62	0.674046	39.90	0.1234	2212	(3 1 1)
81.32	40.66	0.709651	52.10	0.1814	652	(2 2 2)
Y						

© 2026 Reseapro Journals
https://doi.org/10.61577/jnd.2026.100009

Table 1 (continued)

2θ (deg)	θ (deg)	FWHM (radians)	Crystal size, D (nm)	d-spacing (nm)	Intensity,I (cps°)	(h k l)
15.58	7.79	0.135961	78.40	0.5683	100	(0 0 4)
17.13	8.87	0.154811	54.30	0.5172	246	(1 0 3)
29.74	14.87	0.25953	38.40	0.3002	441	(0 1 2)
32.26	16.13	0.281522	58.60	0.2772	271	(0 0 3)
38.08	19.04	0.001395	109.90	0.2361	9744	(1 1 1)
44.26	22.13	0.002182	71.80	0.2045	4633	(2 0 0)
64.41	32.21	0.002007	84.90	0.1445	2880	(2 2 0)
77.36	38.68	0.675093	69.50	0.1232	3195	(3 1 1)
81.49	40.75	0.711222	94.50	0.1180	923	(2 2 2)

Table 1, using equation (1), crystallite sizes for sample X are calculated to be 71.1 nm, 49.6 nm, and 48.8 nm, with an average size of 56.5 nm. In comparison, sample Y shows larger crystallite sizes of 109.9 nm, 71.8 nm, and 84.9 nm, yielding an average size of 88.87 nm. Table 1 indicates that the FWHM values increase with larger 2θ angles and decrease with smaller crystallite sizes.

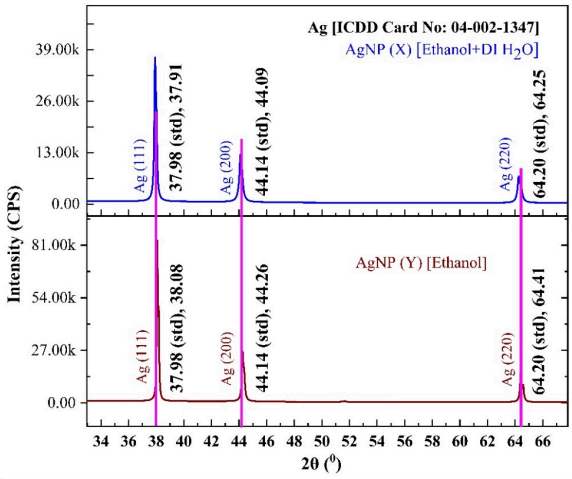


Figure 3. Diffractogram illustration for preferred oriented Ag NPs.

A rightward shift in the 2θ value of an XRD pattern indicates a reduction in the interplanar spacing of the crystal structure. As a result of this compression, the spacing between atomic planes decreases, which necessitates a larger diffraction angle for constructive interference, thereby causing the 2θ value to shift rightward [46]. In Figure 3, the diffraction for synthesized Ag NPs (Y) is observed at 37.91°, 44.09°, and 64.25°, which are shifted to the right of the standard 2θ values of 37.98°, 44.14°, and 64.20° from ICDD [Card No: 04-002-1347] standard data. In contrast, the diffraction for synthesized Ag NPs X at 37.91° and 44.09° is shifted to the left, while the diffraction at 64.25° is shifted to the right of the standard values. Since the 2θ values for Y show a more remarkable rightward shift compared to X, this indicates a reduction in the interplanar spacing in Y, as confirmed by the data presented in **Table 2**.

Table 2. Comparison of experimental and ICDD standard data.

ICDD Card No: [04-002-1347]				Experimental Diffraction Parameters			
2θ	**d-spacing (nm)**	**h k l**	**Lattice parameters of the ICDD standard**	**X (2θ)**	**d-spacing(nm)**	**Y (2θ)**	**d-spacing(nm)**
37.98	0.2367	(1 1 1)	a=b= c= 4.1 Åα=β=γ= 90.0°Space Group: Fm-3m (225).a/b:1.000 and c/b:1.000.	37.91	0.2371	38.08	0.2361
44.14	0.2050	(2 0 0)		44.09	0.2052	44.26	0.2045
64.20	0.1450	(2 2 0)		64.25	0.1448	64.41	0.1445

A comparison between the experimental XRD data and the standard ICDD data [Card No: 04-002-1347] confirms the formation of phase-pure face-centered cubic (FCC) silver NPs. The characteristic diffraction peaks observed at approximately 37.9°, 44.1°, and 64.2° correspond well to the (111), (200), and (220) crystallographic planes of the metallic silver phase, respectively. A close agreement between the experimental and standard d-spacing values indicates high crystallinity and successful phase formation without detectable secondary phases or impurities [47]. Minor shifts in peak positions between samples X and Y suggest slight variations in lattice parameters, which can be attributed to differences in crystallite size and micro-strain induced by the different washing media [48].

Table 3. Simple peak indexing of Ag NPs by Bragg position.

X					
2θ	**θ**	1000 × $\sin^2\theta$	**1000 × $\sin^2\theta$/35.29**	**Reflection**	**Remarks**
37.91	18.96	105.565	3	(1 1 1)	$1^2+1^2+1^2=3$
44.09	22.05	140.937	4	(2 0 0)	$2^2+0^2+0^2=4$
64.25	32.13	282.856	8	(2 2 0)	$2^2+2^2+0=8$
Y					
2θ	**θ**	**1000 × $\sin^2\theta$**	**1000 × $\sin^2\theta$/35.50**	**Reflection**	**Remarks**
38.08	19.04	106.425	3	(1 1 1)	$1^2+1^2+1=3$
44.26	22.13	141.910	4	(2 0 0)	$2^2+0^2+0^2=4$
64.41	32.21	284.114	8	(2 2 0)	$2^2+2^2+0^2=8$

Peak indexing and the corresponding values hold significant importance, as shown in **Table 3.** The calculated profiling values for the Ag phase X are 105.565, 140.937, and

© 2026 Reseapro Journals
https://doi.org/10.61577/jnd.2026.100009

282.856, while for the silver phase Y, they are 106.425, 141.910, and 284.114. These values indicate that the atoms are uniformly distributed across the crystal planes or Miller indices, exhibiting a preferred orientation for constructive interference [49].

Table 4. Peak indexing by d-spacing of Ag NPs.

X					
2θ	**d-spacing (Å)**	**1000/ d^2**	**$(1000/d^2)/59.49$**	**Reflection**	**Remarks**
37.91	2.371	177.884	3	(1 1 1)	$1^2+1^2+1^2=3$
44.09	2.052	237.490	4	(2 0 0)	$2^2+0^2+0^2=4$
64.25	1.448	476.939	8	(2 2 0)	$2^2+2^2+0^2=8$
Y					
2θ	**d-spacing (Å)**	**1000/ d^2**	**$(1000/d^2)/53.16$**	**Reflection**	**Remarks**
38.08	2.361	179.394	3	(1 1 1)	$1^2+1^2+1^2=3$
44.26	2.045	239.119	4	(2 0 0)	$2^2+0^2+0^2=4$
64.41	1.445	478.921	8	(2 2 0)	$2^2+2^2+0^2=8$

The d-spacing values, representing the interplanar spacing between crystal planes, decrease as the diffraction angle (2θ) increases, consistent with Bragg's law, which relates d-spacing to the diffraction angle and the wavelength of the X-rays used [50]. Peak profiling, as shown in **T**able 4, reveals d-spacing values of 177.884, 237.490, and 476.939 for the Ag phase X and 179.394, 239.119, and 478.921 for Ag phase Y. These values confirm the uniform distribution of atoms across the crystal planes in the silver crystal [51].

Table 5. Crystallinity integration of Ag NPs against ICDD standard [04-002-1347] data.

ICDD Card No: [04-002-1347]			Experimental Diffraction Parameters					
Standard			**X**			**Y**		
2θ	**Norm. I. (%)**	**Crystallinity (%)**	**2θ**	**Norm. I. (%)**	**Crystallinity (%)**	**2θ**	**Norm. I. (%)**	**Crystallinity (%)**
37.98	100.00	59.24	37.91	100.00	55.26	38.08	100.00	56.46
44.14	45.70		44.09	49.16		44.26	47.55	
64.20	23.10		64.25	31.80		64.41	29.56	

Table 5 presents the normalized intensity (I %) and crystallinity, where crystallinity percentages were 55.26 % for X Ag NPs and 56.46 % for Y Ag NPs, compared to 59.24 % for the standard ICDD reference sample. Therefore, the X Ag NPs powder exhibits an almost similar alignment with the reference ICDD standard as well as Y Ag NPs.

The crystalline phase percentage was analyzed using Rietveld refinement under WPPF conditions. Figure 4 demonstrates that the WPPF method identifies phase X as consisting of 100 % metallic Ag, while phase Y contains 91.8 % metallic silver and 8.2 % silver nitrate. This indicates that the X phase is the most effective for forming a pure metallic silver phase.

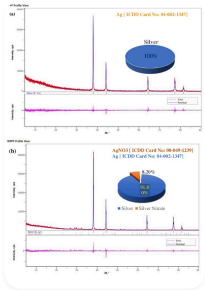


Figure 4. Quantitative analysis of synthesized Ag NPs by the WPPF method.

Table 6. Rietveld's refinement study by the WPPF method of synthesized Ag NPs.

Ag NPs	Lattice parameters	Rp(%)	Rwp (%)	χ^2	S	Strain (%)	Lattice volume ($Å^3$)
X	α=β=γ= 90.0°.a=b=c= 4.09333 Å	10.48	15.20	1.03 53	1.01 75	0.207	68.585
Y	α=β=γ= 90.0°.a=b=c= 4.0874 Å	10.87	15.16	1.24 68	1.11 66	0.119	68.285

Table 6 presents the quantitative analysis of the crystalline phases, specifically the FCC structure of Ag NPs, obtained through Rietveld refinement. The Ag NPs of phase X exhibit a lattice volume of 68.585 $Å^3$, strain of 0.207 %, axial parameters a=b=c= 4.09333 Å, and angular parameters α=β=γ= 90°. In contrast, the Ag NPs of phase Y have a lattice volume of 68.285 $Å^3$, a strain of 0.119 %, axial parameters a=b=c= 4.0874 Å, and angular parameters α=β=γ= 90°. A schematic of the FCC structure of Ag is illustrated in Figure 5. Figure 5 (a) and (b) show the silver FCC structure at the (c) (111), (d) (200), and (e) (220) Miller indices. The structural symmetry was developed by VESTA [visualization system for electronic and structural analysis] software, where considering the parameters were (a=b=c= 4.09333 Å, α=β=γ= 90.0°; x = 0.00000, y = 0.00000, z =0.00000) noted.

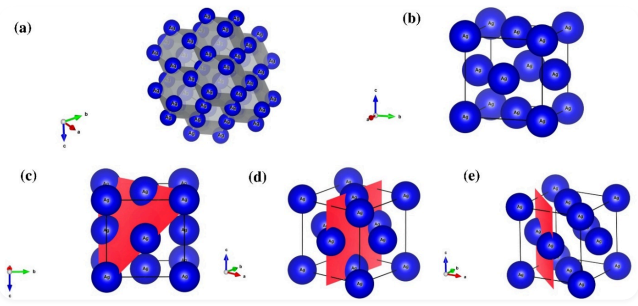


Figure 5. (a) and (b) Ag FCC structure towards the (c) (111), (d) (200) and (e) (220) planes.

The strain curve shown in Figure 6 indicates that the strain of Ag NPs in phase X is 0.207 %, while in phase Y, it is 0.119 %. Lower distortions typically result in a more organized crystal structure, which enhances light-driven efficiency and electrical conductivity [52]. Conversely, higher strain can reduce mechanical strength and light-response activity.

The lattice volume analysis reveals that Ag NPs in phase X

© 2026 Reseapro Journals
https://doi.org/10.61577/jnd.2026.100009

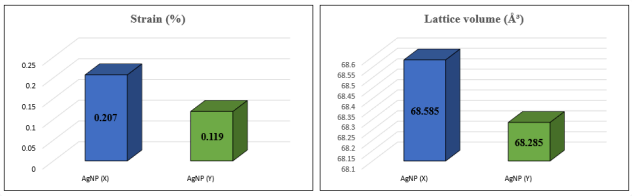


Figure 6. Strain and lattice volume comparison of synthesized Ag NPs.

exhibit a larger lattice volume, 68.525 Å^3, than those in phase Y, 68.285 Å^3. Since the lattice volume of Ag NPs in phase X is higher than that of phase Y, phase X is better suited for these applications. In fact, it introduces surface defects such as dislocations and oxygen vacancies, which serve as active sites for charge separation and adsorption [31,53]. In sample X, the higher intrinsic strain is accompanied by enhanced crystallinity and smaller crystallite size, which together improve the UV-light activity. The strain-induced defect states in X likely facilitate charge trapping and reduce electron-hole recombination, as supported by previous studies on strained metal oxides and silver nanostructures [54].

Crystallographic parameter analysis

Lattice parameters of the silver crystal

Lattice parameters for each diffraction peak position can be calculated using the following equation [41].

$$\frac{1}{d^2} = \frac{\left(h^2 + k^2 + l^2\right)}{a^2} \quad (6)$$

Here, d means interplanar spacing; h, k, and l mean Miller indices; a = Lattice parameter, and $1/d^2$ is the reciprocal square of the interplanar spacing. Table 7 details each diffraction peak lattice value, showing that the average lattice parameters of Ag NPs are 0.4103 nm for phase X and 0.4089 nm for phase Y. So, X has a higher lattice volume, which is responsible for the lattice parameter of the synthesized nanomaterial [55].

Radius of prepared silver nanoparticles

The Ag NPs that are produced have an FCC crystal structure, and we can determine their radius using the following equation [56].

$$a = \frac{4r}{\sqrt{2}} \quad (7)$$

Where **a** is the lattice parameter, **r** is the atomic radius of the Ag atom in the FCC structure, and $\sqrt{2}$ is the geometrical factor associated with the face-centered cubic crystal arrangement. For Ag NPs of X, Radius, (r) = 0.1447 nm. [Unit cell edge, a = 4.09333 Å]. For Ag NPs of Y, Radius (r) = 0.1445 nm. [Unit cell edge, a = 4.0874 Å]. So the X has high mechanical properties that are responsible for the radius of synthesized Ag NPs [57].

Atomic packing factor

The atomic packing factor (APF) is the ratio of the total volume of atomic spheres to the volume of a unit cell [20].

The total volume of atomic spheres, $V_s = 4 \times \frac{4}{3}\pi r^3$ (8)

The volume of the unit cell, $V_c = a^3 = \left(\frac{4r}{\sqrt{2}}\right)^3 = 16r^3\sqrt{2}$ (9)

For Ag NPs of X, r = 0.1447 nm, $V_s = 0.05076$ nm^3, and $V_c = 06856$ nm^3. So, Atomic Packing Factor, $APF = \frac{V_s}{V_c} = \frac{0.05076}{0.06856}$ = 0.74037 = 74.037 %. For Ag NPs of Y, r = 0.1445 nm $V_s = 0.05055$ nm^3 and $V_c = 0682$ nm^3, Atomic Packing Factor, $F = \frac{V_s}{V_c} = \frac{0.05055}{0.06827}$ = 0.74044 = 74.044 %. A higher APF, as observed in phase Y, typically corresponds to denser atomic arrangements, which can enhance mechanical stability and thermal conductivity [58]. The more open structure in X facilitates better dye molecule interaction and electron-hole utilization, validating that reduced packing density (i.e., lower APF) is beneficial for catalytic applications in NPs [17,59].

Table 7. Structural and mechanical properties of Ag NPs.

2θ(deg)	(h k l)	Crystal size, D(nm)	d-spacing(nm)	Lattice parameter, a (nm)	Dislocation density, δ (nm^{-2})	Atomic Packing Factor, (APF)(%)	Intrinsic stress, σ_s (GPa)	Specific Surface area, S (m^2/g)	Surface area to volume ratio
X									
37.91	(111)	71.10	0.2371	0.4106	1.98×10^{-4}	74.037	0.08201	10.11	10.7×10^7
44.09	(200)	49.60	0.2052	0.4104	4.06×10^{-4}				
64.25	(220)	48.80	0.1448	0.4096	4.20×10^{-4}				
Average values		56.50		0.4103	3.41×10^{-4}				
Y									
38.08	(111)	109.90	0.2361	0.4089	8.28×10^{-5}	74.044	0.02743	6.43	6.74×10^7
44.26	(200)	71.80	0.2045	0.4090	1.94×10^{-4}				
64.41	(220)	84.90	0.1445	0.4087	1.39×10^{-4}				
Average values		88.87		0.4089	1.39×10^{-4}				

Surface area to volume ratio of the samples

© 2026 Reseapro Journals
https://doi.org/10.61577/jnd.2026.100009

Surface area of Ag NPs, $SA_{part} = 4\pi R^2$ (10)

Volume of particles, $V_{part} = \frac{4}{3}\pi R^3$ (11)

The synthesized Ag NPs (X) were measured to have a surface area of 10028.75 nm^2 = 10028.75 $\times 10^{-18}$ m^2 and a volume of 94437.4 nm^3 = 94437.4 $\times 10^{-27}$ m^3; the surface area-to-volume ratio is 10.7 $\times 10^7$. In contrast, the synthesized Ag NPs (Y) were measured to have a surface area of 24811.9 nm^2 = 24811.9 $\times 10^{-18}$ m^2 and a volume of 367505.8 nm^3 = 367505.8 $\times 10^{-27}$ m^3; the surface area to volume ratio is 6.74 $\times 10^7$. Therefore, the surface area to volume ratio of the synthesized Ag NPs (X) is significantly larger than the explored highly reactive side of the synthesized NPs [60].

Intrinsic stress () of silver crystal

Intrinsic stress is computed in the nanoparticles for the departure of the observed lattice constant of Ag NPs from the bulk [61].

$$(\sigma_s) = \frac{Y(a - a_0)}{2a_0\gamma} \quad (12)$$

For silver, Young's modulus, Y = 83 GPa, Poisson's ratio, $\gamma = 0.37$. For the Ag NPs of phase X, the lattice constant a is 0.4106 nm, and the bulk lattice constant a_0 is 0.4103 nm. The intrinsic stress of the sample was measured at 0.08201GPa. For the Ag NPs of phase Y, the lattice constant a is 0.4090 nm, and the bulk lattice constant a_0 is 0.4089 nm. The intrinsic stress of the sample was measured at 0.086950 GPa. Where X analyzed the highly stable crystalline phase of the synthesized NPs [59].

Specific surface area (S) of Ag NPs

The specific surface area is related to NPs because as the particle size reduces, the specific surface area reduces. The following equation can be used to determine the specific surface area [42].

$$S = \frac{6 \times 10^3}{D_c \times \rho} \quad (13)$$

Where, S is the Specific surface area, Dc is the average crystallite size, 6 × 10^3 is the Conversion factor derived from the geometrical relationship, and ρ is the Density of the material. The lattice parameters of the face-centered cubic silver phase were determined from the indexed diffraction peaks and were cross-checked against the corresponding interplanar spacings. For a cubic crystal system, the lattice parameter was calculated using $\frac{1}{d^2} = \frac{\left(h^2 + k^2 + l^2\right)}{a^2}$ where d is the interplanar spacing and hkl denotes the Miller indices. The calculated lattice parameters were checked for consistency across the indexed reflections and compared with the values obtained from the crystallographic refinement, where applicable.

Significance of structural parameters in photocatalytic activity

The physical parameters, such as dislocation density (δ), lattice strain (ε), and intrinsic stress (σ), were calculated from the XRD data using standard formulas. The dislocation density was estimated using the relation δ= $1/D^2$, where D is the crystallite size [62]. Several contemporary studies have emphasized that lattice distortion, interfacial charge transfer, and microstructural evolution significantly influence photocatalytic, antimicrobial, electrochemical, and optical properties of NPs [63]. Furthermore, solvent-assisted synthesis and post-treatment conditions have emerged as important parameters governing crystal growth kinetics, phase stability, and defect formation in nanoscale systems [64]. These findings support the importance of systematically investigating solvent-mediated crystallographic modulation in Ag NPs for enhanced functional performance.

Comparison with recent studies

Compared with other green methods, the controlled sol-gel approach provides better control over crystallinity, particle size, and phase purity, while plant-based methods may show inconsistencies due to complex biomolecules [65]. Recent studies have reported photocatalytic efficiencies of 50 to 75 % for Ag NPs under visible or halogen light using plant-mediated synthesis [66]. In comparison, our optimized sample X achieved 82.7 % degradation of methylene blue within 180 min, along with enhanced crystallinity and smaller crystallite size, demonstrating clear performance advantages.

Comparison of MB degradation with reported literature

Several recent studies have reported the photocatalytic degradation efficiency of MB using Ag NPs synthesized via green or sol-gel methods under visible or halogen light. For example, Meenakshi., et al (2021) [64] achieved 64.70 % degradation using Ag NPs synthesized with lemon extract under sunlight after 240 minutes. Salam., et al (2022) [67] reported ~73.0 % MB removal using Ag-TiO_2 composites under halogen light over 200 minutes. Similarly, Arumugam., et al (2014) [68] reported 68.0 % degradation using Ag NPs derived from plant-mediated synthesis within 180 minutes. In contrast, our sample X achieved 82.70 % degradation under halogen light in 180 minutes, outperforming these reports in both efficiency and time.

Average crystallite size calculation analysis

Scherrer model

The Scherrer equation is a formula used in the XRD analysis to estimate the size of crystallites in a material. Equation (1) is particularly useful in the study of nanocrystalline materials [43]. The calculated average crystallite size of samples X and Y was 50.09878 and 73.65 nm, respectively.

W-H model

This method helps distinguish the broadening of diffractions caused by small crystallite sizes from those caused by lattice strain. By applying the following equation, crystallite sizes were calculated [69].

$$\beta cosleft(\theta ight) = \varepsilon(4sinleft(\theta)ight) + \frac{k\lambda}{D} \quad (14)$$

Where β is the FWHM, θ is the Bragg diffraction angle, **ε** is the Microstrain, βcosθ is the total peak broadening contribution, and 4sinθ is the Strain-related component. ε represents the lattice micro-strain. Figure 7 presents the Williamson–Hall plots of samples X and Y, while the calculated crystallite size and strain values are summarized in Table 8. Comparing Equation (3) with the standard equation of the straight line (y= mx + c), we get the mentioned equation.

$$y = \beta cosleft(\theta ight), \quad x = 4sinleft(\theta ight), \quad m = \varepsilon \text{ and } \quad c = \frac{k\lambda}{D} \quad (15)$$

© 2026 Reseapro Journals
https://doi.org/10.61577/jnd.2026.100009

Monshi – Scherrer model

The Monshi-Scherrer method is an adaptation of the traditional Scherrer equation. It also assumes the material is isotropic and homogeneous. By applying the following equation, we calculated crystallite size [50,53].

$$ln(\beta) = ln\frac{1}{cos\theta} + ln\frac{k\lambda}{D} \quad (16)$$

The calculated crystallite size of samples X and Y was 61.11 and 60.78 nm, respectively, in Figure 7(c) and (d).

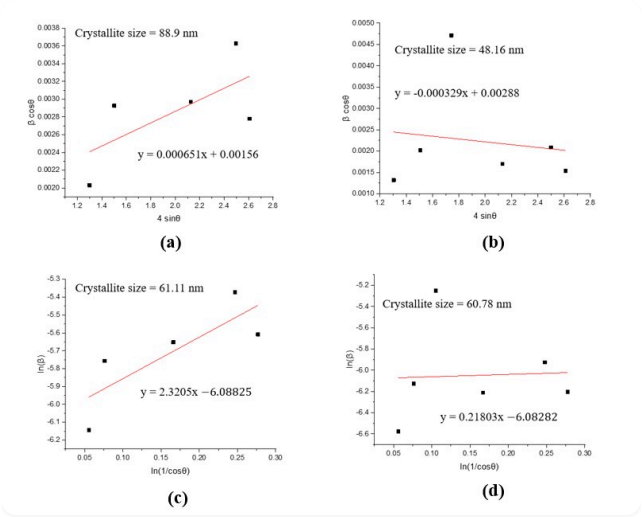


Figure 7. Estimation of crystallite size using Williamson-Hall plot (a) X sample (b) Y sample; using Monshi-Scherrer method (c) X sample and (d) Y sample.

Straight line model

The straight-line method involves plotting the Scherrer equation in a form that allows for a linear fit, making it easier to extract the crystallite size. The required equation is depicted below [53,54].

$$cos\theta = \frac{k\lambda}{D_L} \times \frac{1}{FWHM} \quad (17)$$

The calculated crystallite size of Ag NPs samples X and Y was 192.59 and 1489.85 nm, respectively, as displayed in Figure 8 (a), (b).

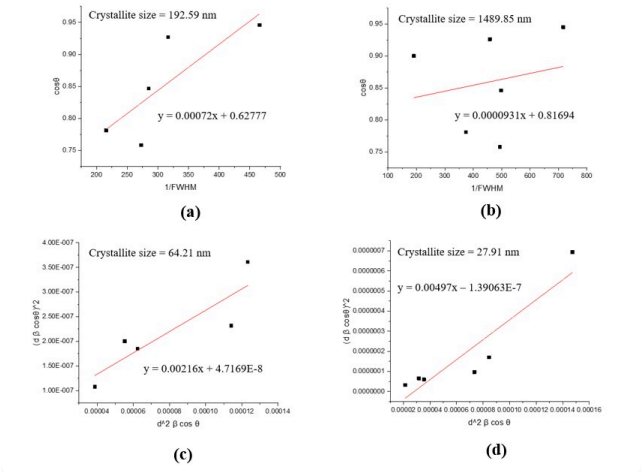


Figure 8. Estimation of crystallite size using linear straight-line model (a) X sample (b) Y sample; Size-strain plot model (c) X sample and (d) Y sample.

Size-Strain plot model

Separating the effects of crystallite size and micro strain on the broadening of diffraction peaks, which can be caused by imperfections and dislocations in the crystal lattice. Assumes uniform strain and isotropic broadening, given equation was employed [49,54].

$$(d\beta cosleft(\theta ight))^2 = \frac{k\lambda}{D}(d^2\beta cosleft(\theta) + \frac{\varepsilon^2}{4}ight) \quad (18)$$

The calculated crystallite sizes of samples X and Y were 64.21 and 27.91 nm, respectively (Figure 8(c), (d)).

Sahadat-Scherrer model

The Sahadat-Scherrer model is a variation of the Scherrer equation, which is commonly used in XRD analysis to estimate the size of crystallites in a material. The given equation was expressed [53,54].

$$cos\theta = \frac{k\lambda}{D_{s-s}} \times \frac{1}{FWHM} \quad (19)$$

Where, Ds−s is the crystallite size calculated using the Sahadat–Scherrer model (nm).

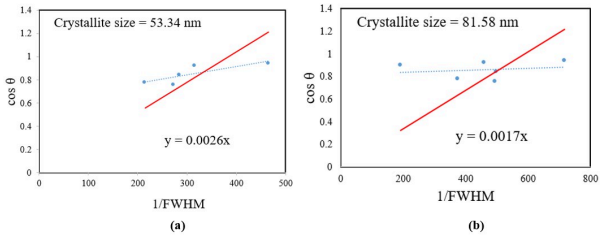


Figure 9. Estimation of crystallite size using the Sahadat-Scherrer model (a) X sample (b) Y sample.

Table 8. Average crystallite size calculation of silver nanoparticles using models.

Name of the Model	Obtained Size		Calculated size	
X (± 0.01)	Y (± 0.01)	X (± 0.01)	Y (±0.01)	
Scherrer Equation	50.09 nm	73.65 nm		
Sahadat-Scherrer Model	53.34 nm	81.58 nm		
Williamson-Hall Plot	88.90 nm	48.16 nm	52.3 nm	73.36 nm
Monshi-Scherrer Method	61.11 nm	60.78 nm		
Linear straight-line Model	192.59 nm	1489.85 nm		
Size-strain plot Model	64.21 nm	27.91 nm		

The average crystallite size of the synthesized silver nanoparticles was evaluated using different X-ray diffraction (XRD)-based approaches. The Debye–Scherrer equation was employed to estimate the apparent crystallite size from the peak broadening, whereas the Williamson–Hall (W–H) method was used to assess the combined contributions of crystallite size and microstrain. The differences between the values obtained from these methods arise from their underlying assumptions and the contributions of lattice strain and instrumental broadening to the observed diffraction-peak

© 2026 Reseapro Journals
https://doi.org/10.61577/jnd.2026.100009

widths. By observing the values, it is found that the Sahadat-Scherrer model is best for compiling in Table 8. The Sahadat-Scherrer model was chosen for compiling the crystallite size and related structural parameters in Table 8 because it builds upon the classical Debye-Scherrer equation but incorporates lattice strain, dislocation density, and other microstructural effects more holistically [70]. Unlike the standard Scherrer equation, which assumes uniform strain-free crystals and ignores dislocations or broadening due to micro-strain, the Sahadat-Scherrer model is designed to address real-world nanocrystalline materials where such imperfections significantly influence diffraction profiles [71]. The crystallite sizes derived using this method aligned well with those obtained from Rietveld refinement, confirming its validity. Furthermore, it avoids underestimations typical of classical Scherrer analysis in strained or non-ideal crystals [72]. Therefore, the use of the Sahadat-Scherrer model is not solely based on numerical proximity, but rather on its theoretical appropriateness for characterizing the strain-rich, defect-containing Ag NPs synthesized under sol-gel conditions. On the other hand, from the linear straight-line model, we got values higher than 100.0 nm. That's why this model is not validated for cubic Ag NPs observation. The influence of washing media on crystallization can be attributed to variations in surface energy driven by solvent polarity, dielectric constant, and hydrogen bonding interactions during the post-synthesis stage. Ethanol, being less polar (dielectric constant 24.3), offers weaker hydrogen bonding compared to distilled water (dielectric constant 78.5), which facilitates stronger hydration and more efficient removal of surface-bound species [21]. In particular, the ethanol-water mixture (sample X) creates a mixed solvent environment that balances solubility and reactivity, effectively lowering surface energy barriers and promoting the formation of highly crystalline structures [63]. Lower surface energy reduces the thermodynamic barrier for atom diffusion and realignment, which favors larger grain domains and fewer defects [39]. Furthermore, based on the Gibbs free energy principle ($\Delta G = \Delta H - T\Delta S$), the entropy-driven contribution of water molecules may promote more ordered nucleation and minimize internal strain [34]. This explains the enhanced crystal quality, reduced crystallite size, and improved phase purity observed in the X sample.

UV spectrophotometry

The UV–visible absorption spectra of the synthesized Ag NPs are presented in Figure 10. The characteristic absorption peaks were observed at 402.18 nm for sample X and 405.60 nm for sample Y, corresponding to the localized surface plasmon resonance (LSPR) of metallic Ag NPs. Typically, Ag NPs exhibit SPR absorption within the range of 400 to 500 nm, depending on particle size, morphology, crystallinity, and surrounding dielectric environment [73].

The slight blue shift observed for sample X indicates the formation of comparatively smaller and more uniformly distributed NPs, which is consistent with the TEM and XRD analyses [74]. In metallic NPs, the LSPR behavior is strongly influenced by particle size and surface electron oscillation. Smaller NPs generally exhibit blue-shifted LSPR peaks due to enhanced surface electron confinement and reduced scattering effects [75,76]. The sharper and more intense LSPR peak of sample X suggests improved nanoscale dispersion and crystallinity compared with sample Y. Enhanced SPR characteristics may facilitate efficient light absorption and

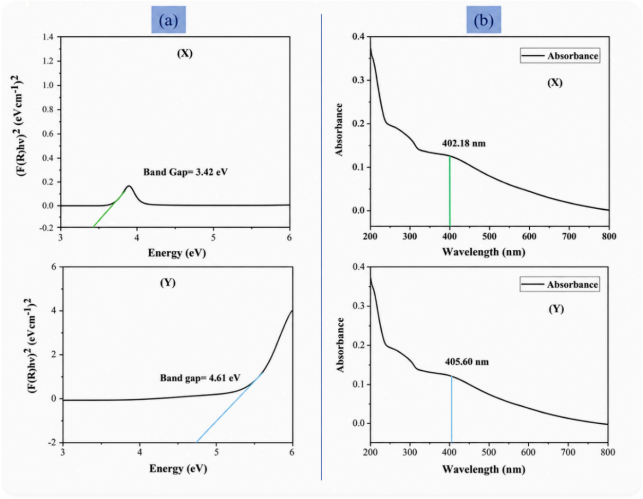


Figure 10. UV absorbance spectra of synthesized AgNPs.

electron transfer during photocatalytic reactions, contributing to the improved methylene blue degradation performance observed for sample X [77].

Zeta potential and dynamic light scattering

The hydrodynamic diameter, a particle's diameter in a colloidal system, corresponds to homogeneous diffusion in Brownian motion. X and Y-produced AgNPs had calculated diameters of 125.6 nm and 267.2 nm, respectively, as shown in Figure 11. The values of X and Y represent the conformation of the particle sizes in a colloidal system in nanoscale fluctuation. The movement of X and Y particles in relation to one another is what causes these fluctuations. In contrast to the Y NPs, the X NPs had a smaller diameter.

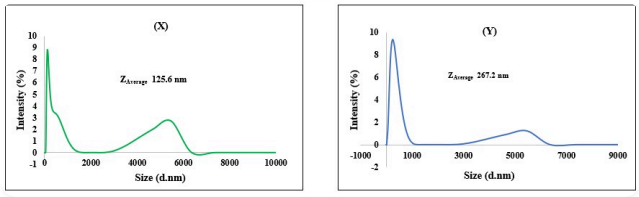


Figure 11. Hydrodynamic diameter of synthesized AgNPs.

The stability of NPs in a suitable medium is indicated by their zeta potential**.** In Figure 12, the X and Y potential values of the synthesized NPs were -20.59 and -13.08 mV, respectively. X particles in the colloidal medium showed good stability.

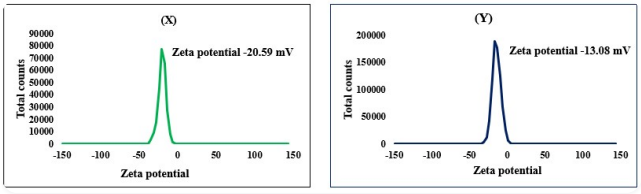


Figure 12. Zeta potential analysis of synthesized Ag NPs.

The high zeta potential of the X particles indicates a strong electrostatic repulsion between the particles in a suspension. When particles in a suspension strongly repel one another, the suspension becomes more stable because the particles are prevented from aggregating and coming together.

© 2026 Reseapro Journals
https://doi.org/10.61577/jnd.2026.100009

Transmission electron microscopy analysis

To investigate the morphology and particle size distribution of the synthesized sample X, TEM analysis was performed at different magnifications. Figure13 (a) and Figure13 (b) present the TEM micrographs recorded at scale bars of 200 nm and 100 nm, respectively. The images reveal the formation of nearly spherical to quasi-spherical NPs with relatively smooth surfaces and well-defined particle boundaries. The particles are distributed throughout the observed region and exhibit nanoscale dimensions with moderate agglomeration, which is commonly observed in nanomaterials due to their high surface energy. Despite some particle-to-particle contact, individual particles remain distinguishable, indicating that the synthesis route successfully produced discrete nanostructures without severe structural coalescence. The contrast variation observed in the micrographs further confirms the presence of uniformly formed nanoparticles with good morphological integrity.

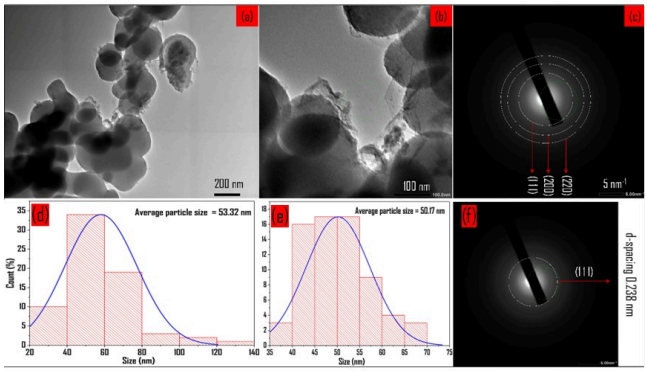


Figure 13. Internal micrograph and crystallographic analysis of Ag NPs.

Figure 13(d) and Figure 13(e) show the particle size distribution histograms, derived from measurements of 50.17 to 53.32 nm NPs. The size distribution is narrow and symmetric, with most particles ranging up to 53.32 nm and average size of 53.32 nm and 50.17 nm, respectively. The distribution profiles exhibit a near-Gaussian behavior, suggesting a relatively narrow particle size distribution and satisfactory uniformity in particle growth during synthesis. The observed nanoscale particle size and relatively narrow distribution indicate effective control over nucleation and growth processes during synthesis [78]. Such NPs possess a high surface-to-volume ratio, which is beneficial for applications requiring enhanced surface activity [79]. Figure 13(c) and Figure 13(f) present the SAED patterns of sample X. The diffraction rings are sharp and well-defined, indexed to the (111), (200), and (220) planes of the FCC structure of the metallic Ag phase. These patterns confirm that the Ag NPs are highly crystalline, with no indication of amorphous phases or oxide impurities. The intensity and clarity of the rings demonstrate a well-ordered atomic arrangement, which is essential for efficient charge transport and reduced electron-hole recombination during photocatalytic activity [39, 74]. The SAED image in Figure 13(f) shows a lattice spacing of 0.238 nm, corresponding to the (111) plane of FCC Ag, confirming the crystalline nature of the Ag NPs. TEM, particle-size analysis, and SAED collectively confirm well-defined Ag NPs with an average size of 50.17–53.32 nm, supporting their enhanced photocatalytic activity toward methylene blue degradation.

Photocatalytic activity on methylene blue dye

Sample X was selected for photocatalytic evaluation on the basis of its smaller crystallite size, higher phase purity, larger specific surface area, and stronger localized surface plasmon resonance (LSPR) absorption. Under halogen-light irradiation, 50 mg of catalyst degraded 10 ppm methylene blue to the extent of 82.69 % within 180 min **Figure 14.**

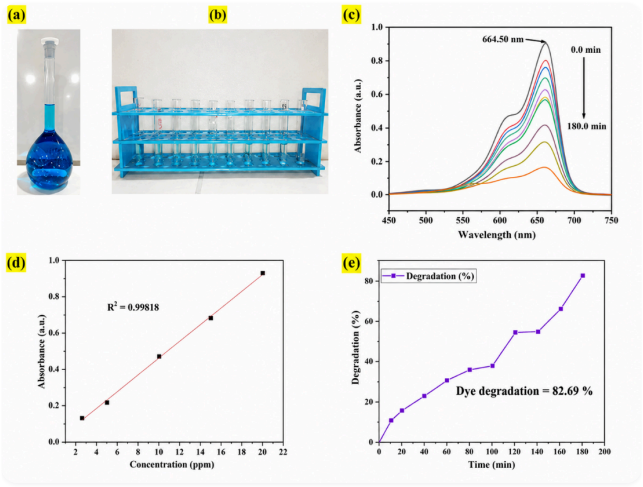


Figure 14. Photocatalytic degradation of MBD (a) dye without AgNPs (b) degradation of MBD with AgNPs in halogen light (c) UV absorption spectrum of MBD treated with AgNPs (d) calibration curve of MBD (e) degradation rate of MBD treated with AgNPs.

These structural and plasmonic properties are favorable for visible-light-driven catalytic activity shown in Figure 14. The UV spectra of MBD degradation after Ag NPs were added under halogen radiation are shown in Figure 14 (c). The dye's absorption at the relevant wavelength gradually decreases with increasing irradiation periods. Using the Beer-Lambert equation, the molar extinction coefficient Ɛ was determined to be 0.025 $Lmg^{-1}cm^{-1}$ after the calibration, which was carried out between 5.0 ppm and 20.0 ppm in Figure 14 (d) [53].

$$A = \varepsilon cl \quad (20)$$

In Equation 06, A stands for absorbance, c for concentration in parts per million, and l for length in centimeters. Under halogen-light irradiation, the Ag NPs exhibited significant photocatalytic degradation of methylene blue dye through a plasmon-assisted catalytic mechanism. The LSPR of Ag NPs triggers collective surface electron oscillations when exposed to visible light, creating energetic hot electrons and localized electromagnetic fields. These excited electrons interact with dissolved oxygen, generating reactive oxygen species (ROS) such as superoxide radicals and hydroxyl radicals, which oxidize and decompose methylene blue molecules into smaller intermediates. Degradation percentage rises with irradiation time, achieving 82.69 % after 180 minutes with sample X due to smaller particle size, better crystallinity, and efficient plasmonic light absorption, as shown by the $\ln(C_0/C)$ vs. time graph. The nearly linear upward trend implies that the degradation adheres to pseudo-first-order kinetic behavior (Figure 15).

As time increases from 0 to 180 minutes, $\ln(C_0/C)$ rises

© 2026 Reseapro Journals
https://doi.org/10.61577/jnd.2026.100009

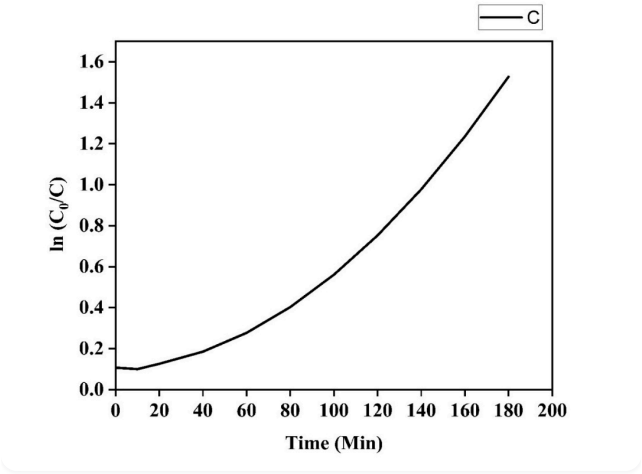


Figure 15. ln(C_0/C) vs time plot for reaction kinetics.

significantly, highlighting the photocatalytic effectiveness of the material in dye removal. Dominant reactive species, superoxide ($\bullet O_2^-$) and hydroxyl radicals (•OH), facilitate methylene blue degradation in plasmonic Ag NPs under visible-light LSPR-induced electron excitation [80]. These radicals can further participate in secondary reactions to produce •OH radicals, and photogenerated holes (h^+) may also contribute to oxidation reactions at the catalyst surface. Therefore, the enhanced photocatalytic performance of sample X can be attributed to efficient reactive species generation and improved charge separation resulting from its smaller crystallite size, higher crystallinity, and enhanced plasmonic absorption.

Nucleation and crystal growth mechanism

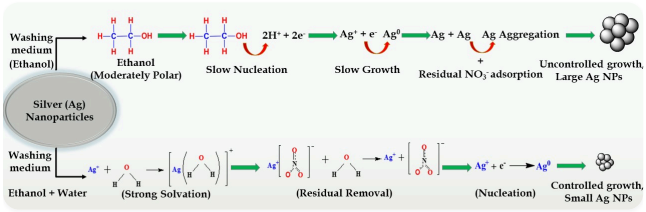


Figure 16. Reaction mechanism of the washing medium on Ag NPs.

Ethanol's moderate polarity in washing limits solvation of ionic species and surface-bound intermediates, leading to weak solvation that encourages electron transfer and reduces Ag^+ availability. This results in fewer nuclei, followed by extended growth and continuous Ag^+ reduction to Ag^0, promoting coalescence and aggregation, ultimately producing larger Ag NPs (Figure 16).

The ethanol-water washing medium enhances dielectric constant and hydrogen bonding, improving Ag^+ ion solvation. This boosts reaction kinetics and homogeneous nucleation, generating numerous nuclei that prevent aggregation, limit growth, and result in uniform, smaller-sized silver nanoparticles. The formation of silver nanoparticles can be discussed in terms of precursor conversion, nucleation, and subsequent particle growth. Under the employed synthesis conditions, the formation of crystalline silver is consistent with the nucleation and growth of Ag nuclei followed by the development of crystalline domains. However, the present structural characterization provides evidence of the final crystalline product rather than direct observation of the nucleation process. Therefore, the proposed mechanism is presented as a plausible interpretation of the experimental findings rather than a conclusively established pathway.

Conclusion

Emphasizes the significance of the washing conditions after the synthesis on the properties of the Ag NPs prepared by the sol-gel method. Two washing media were tested, and XRD with Rietveld refinement showed that FCC metallic Ag was formed in both samples. Sample X, however, exhibited higher phase purity and crystallinity, and sample Y had some silver nitrate residues. The better quality of sample X could be related to the increased polarity and hydrogen-bonding capacity of the ethanol–water medium, which would allow the removal of any residual ionic species and organic residues. Structural characterization also revealed that sample X possessed smaller crystallites, better dispersion, higher surface area, and favorable defect and surface-charge characteristics. TEM and SAED also showed well-dispersed Ag nanoparticles with distinct lattice fringes, which are characteristic of the FCC Ag structure. Furthermore, sample X showed better SPR properties and better optical behavior. It also had better photocatalytic activity, with 82.69 % degradation of methylene blue after 180 min of irradiation with halogen light. This increased activity may be correlated with its smaller crystallite size, better crystallinity, higher number of active sites, and better charge separation. In general, the results demonstrate that a simple and scalable modification of the washing medium constitutes an effective means of tuning the crystallographic and functional properties of sol–gel-derived silver nanoparticles for environmental applications.

Acknowledgement

The author heartily thanks the authority of BCSIR, Bangladesh, and Dr. Samina Ahmed, CSO and Director (addl. charge), IGCRT, BCSIR, for permission and access to the laboratories under the thesis work '*Plat mediated synthesis and bioactivity of silver nanoparticles using Callirtemon Branchyandrms (bottle brush) plants (leaves, flower, stems)*'. We also express our gratitude to the thesis co-supervisor for her outstanding cooperation, the laboratory's facilities, mentor, and scientific advisor of this manuscript.

Ethics Approval and Consent to Participate

Ethical approval was not required for this study because it involved only the synthesis and characterization of silver nanoparticles and the photocatalytic degradation of methylene blue, without the use of human participants, human samples, animals, or personally identifiable data.

Declaration of Competing Interests

The authors declare no competing financial or personal interests that could have influenced this work.

Author Contribution

Sumaiya Islam Sadia: Data curation, formal analysis, investigation, methodology, resources, software, validation, writing original draft.

Kamrun Nahar: Data curation, Software.

Mohshin Maola: Resources, software, validation, writing

© 2026 Reseapro Journals
https://doi.org/10.61577/jnd.2026.100009

original draft

Sukanta Mondal: Resources, software, writing original draft

Md. Ashraful Alam: Conceptualization, data curation, formal analysis, methodology, resources, visualization, writing – original draft. Writing review & editing.

Sharif Md. Al-Reza: Data curation, formal analysis, project administration, supervision. visualization. Writing original draft

Raton Kumar Bishwas: Data curation, formal analysis

Shirin Akter Jahan: Conceptualization, data curation, project administration, supervision. Visualization,

writing review & editing

References

1. Alam MA, Munni SA, Mostafa S, Bishwas RK, Jahan SA. An investigation on synthesis of silver nanoparticles. Asian J Res Biochem. 2023;12(3):1–10. https://doi.org/10.9734/ajrb/2023/v12i3234
2. Ahamed MS, Ali MS, Ahmed S, Sadia SI, Islam MR, Rahaman MA, et al.. Synthesis of silver nanomaterials capping by fruit-mediated extracts and antimicrobial activity: A critical review. Int Res J Pure Appl Chem. 2024;25(1):45–60. https://doi.org/10.9734/irjpac/2024/v25i1844
3. Shishir MKH, Sadia SI, Ahmed S, Aidid AR, Rana MM, Hasan MM, et al.. Transmission electron microscopic and X-ray diffraction based study of crystallographic bibliography demonstrated on silver, copper and titanium nanocrystals: State of the art statical review. Asian J Appl Chem Res. 2024;15(3):1–19. https://doi.org/10.9734/ajacr/2024/v15i3287
4. Abbas R, Luo J, Qi X, Naz A, Khan IA, Liu H, et al.. Silver Nanoparticles: Synthesis, Structure, Properties and Applications. Nanomaterials. 2024;14(17):1425. https://doi.org/10.3390/nano14171425
5. Willert M, Rothe R, Landfester K, Antonietti M. Synthesis of Inorganic and Metallic Nanoparticles by Miniemulsification of Molten Salts and Metals. Chem Mater. 2001;13(12):4681–4685. https://doi.org/10.1021/cm011121g
6. Jeon H, Yi S, Oh S. Preparation and antibacterial effects of Ag–SiO2 thin films by sol–gel method. Biomaterials. 2003;24(27):4921–4928. https://doi.org/10.1016/s0142-9612(03)00415-0
7. Shahjahan M, Hasibur Rahman M, Sajjad Hossain M, Afroza Khatun M, Islam A, Hosney Ara Begum M. Synthesis and characterization of silver nanoparticles by sol-gel technique. Nanoscience and Nanometrology. 2017;3(1):34–39. https://doi.org/10.11648/j.nsnm.20170301.16
8. Kotthaus S, Gunther BH, Hang R, Schafer H. Study of isotropically conductive bondings filled with aggregates of nano-sited Ag-particles. IEEE Transactions on Components, Packaging, and Manufacturing Technology: Part A. 1997;20(1):15–20. https://doi.org/10.1109/95.558539
9. Luo Z, Geng H, Zhang X, Du B, Ding E, Wang J, et al.. A timesaving, low-cost, high-yield method for the synthesis of ultrasmall uniform graphene oxide nanosheets and their application in surfactants.. IOPscience. 2026;27(5):055601. https://doi.org/10.1088/0957-4484/27/5/055601
10. Colvin VL, Schlamp MC, Alivisatos AP. Light-emitting diodes made from cadmium selenide nanocrystals and a semiconducting polymer. Nature. 1994;370(6488):354–357. https://doi.org/10.1038/370354a0
11. Tabassum M, Alam MA, Mostofa S, Bishwas RK, Sarkar D, Jahan SA. Synthesis and crystallinity integration of copper nanoparticles by reaction medium. J Cryst Growth. 2024;626:127486. https://doi.org/10.1016/j.jcrysgro.2023.127486
12. Alam MA, Tabassum M, Mostofa S, Kumar Bishwas R, Sarkar D, Akter Jahan S. The effect of precursor concentration on the crystallinity synchronization of synthesized copper nanoparticles. J Cryst Growth. 2023;621:127386. https://doi.org/10.1016/j.jcrysgro.2023.127386
13. Meyers MA, Mishra A, Benson DJ. Mechanical properties of nanocrystalline materials. Prog Mater Sci. 2006;51(4):427–556. https://doi.org/10.1016/j.pmatsci.2005.08.003
14. Cho K, Park J, Osaka T, Park S. The study of antimicrobial activity and preservative effects of nanosilver ingredient. Electrochimica Acta. 2005;51(5):956–960. https://doi.org/10.1016/j.electacta.2005.04.071
15. Iravani S. Green synthesis of metal nanoparticles using plants. Green Chem. 2011;13(10):2638. https://doi.org/10.1039/c1gc15386b
16. Giannini C, Ladisa M, Altamura D, Siliqi D, Sibillano T, De Caro L. X-ray diffraction: A powerful technique for the multiple-length-scale structural analysis of nanomaterials. Crystals. 2016;6(8):87. https://doi.org/10.3390/cryst6080087
17. Sadia SI, Shishir MKH, Ahmed S, Alam MA, Al-Reza SM, Afrin S, et al.. Green synthesis of crystalline silver nanoparticle by bio-mediated plant extract: A critical perspective analysis. Nano-Struct Nano-Objects. 2024;39:101272. https://doi.org/10.1016/j.nanoso.2024.101272
18. Sastry M, Ahmad A, Khan MI, Kumar R. Biosynthesis of metal nanoparticles using fungi and actinomycete. Curr Sci. 2003;85(2):162–170
19. Khatun N, Rini EG, Shirage P, Rajput P, Jha SN, Sen S. Effect of lattice distortion on bandgap decrement due to vanadium substitution in TiO2 nanoparticles. Mater Sci Semicond Process. 2016;50:7–13. https://doi.org/10.1016/j.mssp.2016.04.002
20. Blazhynska MM, Kyrychenko A, Kalugin ON. Molecular dynamics simulation of the size-dependent morphological stability of cubic shape silver nanoparticles. Mol Simul. 2018;44(12):981–991. https://doi.org/10.1080/08927022.2018.1469751
21. Zahan N, Sachchu MMH, Maola M, Islam MT, Islam MR, Biswas A, et al.. X-ray diffraction pattern profiling and sustainable production of crystalline nano-cellulose acetate from waste cotton linter: Crystallite size analysis insights. Int J Sci Res Arch. 2026;19(1):464–477. https://doi.org/10.30574/ijsra.2026.19.1.0683
22. Huang Q, Xia Y. Seeing is believing: How does the surface of silver nanocubes from a polyol synthesis change during sample collection, washing, and redispersion. Langmuir. 2025;41(30):20272–20279. https://doi.org/10.1021/acs.langmuir.5c02610
23. Khan Z, AL-Thabaiti SA, Obaid AY, Khan ZA, Al-Youbi AO. Effects of solvents on the stability and morphology of CTAB-stabilized silver nanoparticles. Colloids Surf A Physicochem Eng Asp. 2011;390(1-3):120–125. https://doi.org/10.1016/j.colsurfa.2011.09.015
24. Hong KH, Park JL, Sul IH, Youk JH, Kang TJ. Preparation of antimicrobial poly(vinyl alcohol) nanofibers containing silver nanoparticles - Hong - 2006 - Journal of Polymer Science Part B: Polymer Physics -. J Polym Sci, Part B: Polym Phys. 2006;44(17):2468-2474. https://doi.org/10.1002/polb.20913
25. Alam MA, Sadia SI, Shishir MKH, Bishwas RK, Ahmed S, Al-Reza SM, et al.. Crystallinity integration and crystal growth behavior study of preferred oriented (111) cubic silver nanocrystal. Inorg Chem Commun. 2025;173:113834. https://doi.org/10.1016/j.inoche.2024.113834
26. Zhang X, Liu Z, Shen W, Gurunathan S. Silver Nanoparticles: Synthesis, Characterization, Properties, Applications, and Therapeutic Approaches. Int J Mol Sci. 2026;17(9):1534. https://doi.org/10.3390/ijms17091534
27. Bansal V, Li V, O'Mullane AP, Bhargava SK. Shape dependent electrocatalytic behaviour of silver nanoparticles. Cryst Eng Comm. 2010;12(12):4280. https://doi.org/10.1039/c0ce00215a
28. Kis VK, Kovács Z, Czigány Z. Improved Method for Electron Powder Diffraction-Based Rietveld Analysis of Nanomaterials. . 2026;14(5):444. https://doi.org/10.3390/nano14050444
29. Nahi O, Kulak AN, Broad A, Xu Y, O'Shaughnessy C, Cayre OJ, et al.. Solvent-Mediated Enhancement of Additive-Controlled Crystallization. Cryst Growth Des. 2026;21(12):7104-7115.. https://doi.org/10.1021/acs.cgd.1c01002
30. Shanbhag VV, Prashantha SC, Ravi kumar CR, Kumar P, Surendra BS, Nagabhushana H, et al.. Comparative analysis of electrochemical performance and photocatalysis of SiO2 coated CaTiO3:RE3+ (Dy, Sm), Li+ core shell nano structures. Inorg Chem Commun. 2021;134:108960. https://doi.org/10.1016/j.inoche.2021.108960
31. Naik R, Prashantha SC, Nagabhushana H, Naik YV, Girish KM, Premkumar HB. Photoluminescent and thermoluminescent properties of low temperature synthesized Nd3+ doped Mg2SiO4 nanophosphors for display and dosimetry applications. Optik. 2019;180:8–19. https://doi.org/10.1016/j.ijleo.2018.11.069
32. . Sr and Fe substituted LaCoO3 nano perovskites: Electrochemical energy storage and sensing applications. J Energy Storage. 2026;89. https://doi.org/10.1016/j.est.2024.111724
33. Gui X, Song B, Chen M, Xu X, Ren Z, Li X, et al.. Soil colloids affect the

© 2026 Reseapro Journals
https://doi.org/10.61577/jnd.2026.100009

aggregation and stability of biochar colloids. Sci Total Environ. 2021;771:145414.
https://doi.org/10.1016/j.scitotenv.2021.145414

34. Jain J, Arora S, Rajwade JM, Omray P, Khandelwal S, Paknikar KM. Silver Nanoparticles in Therapeutics: Development of an Antimicrobial Gel Formulation for Topical Use. Mol Pharm. 2026;6(5):1388–1401.
https://doi.org/10.1021/mp900056g
35. Moynihan HA, Horgan DE. Impurity Occurrence and Removal in Crystalline Products from Process Reactions. Org Process Res Dev. 2017;21(5):689–704.
https://doi.org/10.1021/acs.oprd.6b00403
36. Epifani M, Giannini C, Tapfer L, Vasanelli L. Sol–Gel Synthesis and Characterization of Ag and Au Nanoparticles in SiO2, TiO2, and ZrO2 Thin Films. J Am Ceram Soc. 2000;83(10):2385–2393.
https://doi.org/10.1111/j.1151-2916.2000.tb01566.x
37. Al-Mahmud MR, Hossain Shishir MK, Ahmed S, Tabassum S, Islam Sadia S, Haque Sachchu MM, et al.. Stoichiometry crystallographic phase analysis and crystallinity integration of silver nanoparticles: A Rietveld refinement study. Journal of Crystal Growth. 2024;643:127815.
https://doi.org/10.1016/j.jcrysgro.2024.127815
38. Biswas A, Maola M, Islam MM, Mondal S, Sachchu MMH, Tandra N, et al.. Strategic Roadmap for Exploring Phytochemical Profiles of Ixora nigricans L. Flowers and Leaves Extract: The X-ray Diffraction Overview Insight. J Biol Nat. 2026;18(1):569–586.
https://doi.org/10.56557/joban/2026/v18i110571
39. Umalas M, Vlassov S, Polyakov B, Dorogin LM, Saar R, Kink I, et al.. Electron beam induced growth of silver nanowhiskers. J Cryst Growth. 2015;410:63–68.
https://doi.org/10.1016/j.jcrysgro.2014.10.021
40. Fatimah S, Ragadhita R, Husaeni DFA, Nandiyanto ABD. How to calculate crystallite size from X-Ray Diffraction (XRD) using Scherrer method. ASEAN J Sci Eng. 2021;2(1):65–76.
https://doi.org/10.17509/ajse.v2i1.37647
41. Holzwarth U, Gibson N. The Scherrer equation versus the 'Debye-Scherrer equation'. Nat Nanotech. 2011;6(9):534–534.
https://doi.org/10.1038/nnano.2011.145
42. Alam MA, Hossain Shishir MK, Sarkar D, Bishwas RK, Jahan SA. X-ray line diffraction study of preferred oriented hexagonal zincite nanocrystals: A crystallographic investigation. J Cryst Growth. 2025;666:128230.
https://doi.org/10.1016/j.jcrysgro.2025.128230
43. Yang L, He R, Chai J, Qi X, Xue Q, Bi X, et al.. Synthesis Strategies for High Entropy Nanoparticles. Adv Mat. 2024;37(1):2412337.
https://doi.org/10.1002/adma.202412337
44. Wani IA, Ganguly A, Ahmed J, Ahmad T. Silver nanoparticles: Ultrasonic wave assisted synthesis, optical characterization and surface area studies. Mat Lett. 2011;65(3):520–522.
https://doi.org/10.1016/j.matlet.2010.11.003
45. Muniz FTL, Miranda MAR, Morilla dos Santos C, Sasaki JM. The Scherrer equation and the dynamical theory of X-ray diffraction. Acta Cryst A. 2016;72(3):385–390.
https://doi.org/10.1107/s205327331600365x
46. Ameh ES. A review of basic crystallography and x-ray diffraction applications. Int J Adv Manuf Technol. 2019;105(7):3289–3302.
https://doi.org/10.1007/s00170-019-04508-1
47. Bhadra S, Khastgir D. Determination of crystal structure of polyaniline and substituted polyanilines through powder X-ray diffraction analysis. Polymer Testing. 2008;27(7):851–857.
https://doi.org/10.1016/j.polymertesting.2008.07.002
48. Shreyash N, Bajpai S, Khan MA, Vijay Y, Tiwary SK, Sonker M. Green Synthesis of Nanoparticles and Their Biomedical Applications: A Review. ACS Appl Nano Mater. 2021;4(11):11428–11457.
https://doi.org/10.1021/acsanm.1c02946
49. Kobir MM, Tabassum S, Ahmed S, Sadia SI, Alam MA. Crystallographic Benchmarking on Diffraction Pattern Profiling of Polymorphs-TiO2 by WPPF for Pigment and Acrylic Paint. Arch Curr Res Int. 2024;24(1):62–70.
https://doi.org/10.9734/acri/2024/v24i1623
50. Toraya H. Introduction to X-ray analysis using the diffraction method. Rigaku J. 2016;32(2):35-43
51. Jadhav S, Jadkar A, Mote N, Tamse S, Gosar A, Mahajan D. Impact of Preferred Orientation and Strain on Olopetadine HCL by Using XRD Technique. Asian J Appl Chem Res. 2023;14(4):17–22.
https://doi.org/10.9734/ajacr/2023/v14i4273
52. Rajender G, Giri PK. Strain induced phase formation, microstructural evolution and bandgap narrowing in strained TiO2 nanocrystals grown by ball milling. J Alloys Compd. 2016;676:591–600.
https://doi.org/10.1016/j.jallcom.2016.03.154
53. Farooqi MA, Bae S, Kim S, Bae S, Kausar F, Farooqi HMU, et al.. Eco-friendly synthesis of bioactive silver nanoparticles from black roasted gram (Cicer arietinum) for biomedical applications. Sci Rep. 2026;14(1):22922.
https://doi.org/10.1038/s41598-024-72356-5
54. Liu X, Hu A, Liu Z, Ding K, Xia W, Shangguan H, et al.. Review on Fundamental and Recent Advances of Strain Engineering for Enhancing Photocatalytic CO2 Reduction. Adv Energy Mater. 2024;15(15):2405320.
https://doi.org/10.1002/aenm.202405320
55. Reverchon E, Della Porta G, Sannino D, Ciambelli P. Supercritical antisolvent precipitation of nanoparticles of a zinc oxide precursor. Powder Technology. 1999;102(2):127–134.
https://doi.org/10.1016/s0032-5910(98)00207-1
56. Kainz MP, Legenstein L, Holzer V, Hofe S, Kaltenegger M, Resel R, et al.. (IUCr) GIDInd: an automated indexing software for grazing-incidence X-ray diffraction data." Accessed: May 20. J Appl Crystallogr. 2026;54(4):1256-1267.
https://doi.org/10.1107/S1600576721006609
57. Guo Y, Huang S, Guo Y, Ye Z, Nan J, Zhou Q, et al.. Efficient degradation of organic pollutants by enhanced interfacial internal electric field induced via various crystallinity carbon nitride homojunction. Appl Catal B: Environ. 2022;312:121388.
https://doi.org/10.1016/j.apcatb.2022.121388
58. Song X, Zhang Y, Abdel-Ghafar HM, Abdel-Aal EA, Huang M, Gul S, et al.. Polyamide membrane with an ultrathin GO interlayer on macroporous substrate for minimizing internal concentration polarization in forward osmosis. Chem Eng J. 2021;412:128607.
https://doi.org/10.1016/j.cej.2021.128607
59. Devi TA, Sivaraman RM, Sheeba Thavamani S, Peter Amaladhas T, AlSalhi MS, Devanesan S, et al.. Green synthesis of plasmonic nanoparticles using Sargassum ilicifolium and application in photocatalytic degradation of cationic dyes. Environmental Research. 2022;208:112642.
https://doi.org/10.1016/j.envres.2021.112642
60. Alam MA, Bishwas RK, Mostofa S, Jahan SA. Crystallographic phase stability of nanocrystalline polymorphs TiO2 by tailoring hydrolysis pH. South African Journal of Chemical Engineering. 2024;49:73–85.
https://doi.org/10.1016/j.sajce.2024.04.007
61. Resendiz LR, Tahawy ME, Zhang T, Rossi MC, Cardona DM, Yang T, et al.. Heterostructured stainless steel: Properties, current trends, and future perspectives. Mater Sci Eng R Rep. 2026;150:100691.
https://doi.org/10.1016/j.mser.2022.100691
62. Dridi R, Dridi D, Hammami S, Dimassi W, Chtourou R, Amlouk M. Growth and physical investigations on NiWO4 thin films as a potential for NO2 sensing. Optik. 2023;273:170330.
https://doi.org/10.1016/j.ijleo.2022.170330
63. Shishir MKH, Akand MS, Maola M, Monira MF, Rifat M, Sayeem NR, et al.. Photocatalytic removal of textile dyes: Analytical strategies for post-degradation evaluation. Desalination. 2026;617:119437.
https://doi.org/10.1016/j.desal.2025.119437
64. Cao X, Zhi L, Jia Y, Li Y, Zhao K, Cui X, et al.. A Review of the Role of Solvents in Formation of High-Quality Solution-Processed Perovskite Films. ACS Applied Materials & Interfaces. 2019;11(8):7639–7654.
https://doi.org/10.1021/acsami.8b16315
65. Ahmed S, Shishir MKH, Islam MT, Rahaman MA, Aman S, Aidid AR, et al.. Crystallinity integration of anatase (TiO2) nanocrystal by whole powder pattern fitting (WPPF) method: A Rietveld refinement study. Results Mater. 2025;26:100673.
https://doi.org/10.1016/j.rinma.2025.100673
66. Aidid AR, Shishir MKH, Rahaman MA, Islam MT, Mukta M, Alam MA. Powder X-ray line diffraction pattern profiling of anatase-quartz binary oxide: A crystallographic investigation. Next Materials. 2025;8:100571.
https://doi.org/10.1016/j.nxmate.2025.100571
67. León ER, Palomares RI, Navarro RE, Urbina RH, Tánori J, Palomares CI, et al.. Synthesis of silver nanoparticles using reducing agents obtained from natural sources (Rumex hymenosepalus extracts). Nanoscale Res Lett. 2026;8(1):318
68. Yusoff R, Shamiri A, Aroua MK, Ahmady A, Shafeeyan MS, Lee WS, et al.. Physical properties of aqueous mixtures of N-methyldiethanolamine (MDEA) and ionic liquids. J Ind Eng Chem. 2014;20(5):3349–3355.
https://doi.org/10.1016/j.jiec.2013.12.019
69. Islam M, Islam MT, Shishir MKH, Rahaman MA, Ahmed S, Sadia SI, et al.. X-ray crystallographic structural Profiling of Polyvinyl Alcohol (PVA) caped Nickel Oxide Nanoparticle. Nano Trends. 2025;10:100106.
https://doi.org/10.1016/j.nwnano.2025.100106
70. Himabindu B, Latha Devi NSMP, Rajini Kanth B. Microstructural parameters from X-ray peak profile analysis by Williamson-Hall models;

© 2026 Reseapro Journals
https://doi.org/10.61577/jnd.2026.100009

A review. Mater Today: Proc. 2021;47:4891–4896.
https://doi.org/10.1016/j.matpr.2021.06.256

71. Zhao Y, Zhang J. (IUCr) Microstrain and grain-size analysis from diffraction peak width and graphical derivation of high-pressure thermomechanics. J Appl Crystallogr. 2026;41(6):1095-1108.
https://doi.org/10.1107/S0021889808031762
72. Monshi A, Foroughi MR, Monshi MR. Modified Scherrer Equation to Estimate More Accurately Nano-Crystallite Size Using XRD. World Journal of Nano Science and Engineering. 2012;2(3):154–160.
https://doi.org/10.4236/wjnse.2012.23020
73. Fellah L, Diha A, Boumerzoug Z. Influence of heating temperature on the aluminum used for electric cables. AIP Conf Proc. 2017;1899:030006.
https://doi.org/10.1063/1.5009851
74. Shafi PM, Bose AC. Impact of crystalline defects and size on X-ray line broadening: A phenomenological approach for tetragonal SnO2 nanocrystals. . 2015;5(5).
https://doi.org/10.1063/1.4921452
75. Chen H, Govindasamy C, Oh D, Chelliah R, Ramamoorthy A, Rengarajan T, et al.. Synthesis of SnO2-Sodium alginate-polyethylene glycol-crocin nanocomposite for enhanced antimicrobial and anticancer activity. J Drug Deliv Sci Technol. 2024;93:105449.
https://doi.org/10.1016/j.jddst.2024.105449
76. Muiva C, Sebuso DP, Muchuweni E. Microstructural and optical properties of nanostructured Al/Ag co-doped ZnO thin films (AgxAl0.03ZnO0.97-x) by spray pyrolysis for optoelectronic applications. Phys B: Condens Matter. 2024;690:416206.
https://doi.org/10.1016/j.physb.2024.416206
77. Huo Y, Wang Z, Zhang J, Liang C, Dai K. Ag SPR-promoted 2D porous g-C3N4/Ag2MoO4 composites for enhanced photocatalytic performance towards methylene blue degradation. Appl Surf Sci. 2018;459:271–280.
https://doi.org/10.1016/j.apsusc.2018.08.005
78. Mourdikoudis S, Pallares RM, Thanh NTK. Characterization techniques for nanoparticles: comparison and complementarity upon studying nanoparticle properties.. Nanoscale. 2018;10(27):12871–12934.
https://doi.org/10.1039/c8nr02278j."
79. Ghosh SK, Pal T. Interparticle Coupling Effect on the Surface Plasmon Resonance of Gold Nanoparticles: From Theory to Applications. Chem Rev. 2026;107(11):4797–4862.
https://doi.org/10.1021/cr0680282
80. Hang Y, Wang A, Wu N. Plasmonic silver and gold nanoparticles: shape- and structure-modulated plasmonic functionality for point-of-caring sensing, bio-imaging and medical therapy. Chem Soc Rev. 2024;53(6):2932–2971.
https://doi.org/10.1039/d3cs00793f

© 2026 Reseapro Journals
https://doi.org/10.61577/jnd.2026.100009